Synthesis and tribocorrosion performances of multilayer (Ta/ZrN) n coatings

Nasser Eddine Beliardouh [a,*], Chems Eddine Ramoul [a,b], Corinne Nouveau [c], Emrullah Hakan Kaleli [d], Alex Montagne [e]

[a] Laboratoire d'Ingénierie des Surfaces (LIS), Université BADJI Mokhtar (UBMA), BP 12, 23000, Annaba, Algeria
[b] Research Center in Industrial Technologies CRTI P.O. Box 64, Cheraga 16014 Algiers, Algeria
[c] Arts et Métiers, Institute of Technology, LaBoMaP, HESAM Université, F-71250 Cluny, France
[d] Yildiz Technical University, Faculty of Mechanical Engineering, Automotive Division 34349, E1 Block, No.28, Beşiktaş-Yıldız-İstanbul, TURKEY
[e] Arts et Métiers, Institute of Technology, MSMP, HESAM Université, F-59000 Lille, France

Keywords:
Multilayer coating, Biomaterial, Tribocorrosion
Tantalum
Zirconium nitride
Magnetron sputtering

A B S T R A C T

Multilayer thin coatings (~3 μm in thickness) were deposited using reactive radio frequency magnetron sputtering on Ti-6Al-4 V substrate for biomaterial applications. Films are a combination of hard zirconium nitride with pure tantalum, used to manage interfacial stress and to avoid crack growth. Alternating hard/ductile material is a biomimetic design inspired by nature (nacre-inspired materials). Tribocorrosion tests were performed in Hank's solution at 37 °°C, under open circuit potential by using a ball-on-disk reciprocating tribometer. A tendency to high resistance against corrosion was found for all the samples. Coatings with a top 100 nm thick ZrN layer showed more noble potential as well as a reduction of both the friction coefficient and the wear rate during the sliding phase. The principal wear mechanism is related to a tribocorrosion layer formation.

1. Introduction

Orthopedic prosthesis for arthroplasty are generally manufactured from bulk metal alloys (Ti-6Al-4 V, Cr-Co-Mo…) covered with ceramic-based metal coatings such as nitrides, carbides, and oxides of transition metals (Ti, Zr, Ta). However, the main concern about metallic implants are the generation of wear particles and the release of metallic ions in toxic concentrations. Artificial joints particularly, suffer abrasion wear, fatigue, adhesion, and tribochemical reactions. Consequently, inflammation of surrounding tissues and loosening of implants can occur [1–2]. As the health of patients and the service life of the prosthesis are the fundamental priorities, the implant material has to have simultaneously sufficient mechanical strength, high corrosion resistance, and excellent biocompatibility.

Overall, ceramic-based metal coatings are hard enough to avoid abrasive wear and present a high resistance against corrosion in addition to suitable biocompatibility. That is why the protection of metallic prostheses by ceramic films was recognized as an acceptable first solution. Improvements in design, new manufacturing processes, and surface treatments of several biomedical prostheses are suggested in the literature as solutions to further minimizing risks of implant rejection.

Direct current or Radio Frequency (RF) magnetron sputtering is a cost-efficient method and an excellent way to produce high quality and high-purity (homogeneous) thin films, with strong adhesion to the substrate [1]. This technique can deposit various reactive sputtered coatings, such as transition metal nitrides, oxides, carbides, etc. Sputtered coatings are found to be suitable for many industrial applications due to their unique combination of physical, mechanical, and chemical properties.

Nowadays, multilayered multicomponent coatings are widely used in modern biomaterials science [3]. Several multilayered coatings for biomedical applications are proposed in the literature. Among them, those alternating metallic/ceramic layers such as (Ti/TiN) [4], Ta/TaN [5] *i.e.* (Me/MeN)n. Where "Me" is metal and "n" is the number of alternating bilayers. Nevertheless, ceramic coatings are hard and brittle which is why a combination with a softer metal (Cr, Ti, Ta, and Zr) as an interlayer is recommended to manage interfacial stress and to avoid crack growth.

Zirconium nitride (ZrN) and pure tantalum (Ta) coatings have proven their effectiveness as biomedical materials [6–7]. ZrN coatings

* Corresponding author:
E-mail address: beliardouh_23@yahoo.fr (N.E. Beliardouh).

https://doi.org/10.1016/j.tsf.2022.139184

show excellent mechanical properties; the values of elastic modulus (E) are in the range from 260 GPa to 330 GPa [8–9] and hardness (H) varies from 13 [9] to 30 GPa [8]. Mechanical properties and tribological performances of the ZrN coatings are closely related to microstructure and nitrogen flow during the sputtering process [8]. A specific wear rate in the order of 10^{-7} (mm^3/N.m) was reported by Auger et al. [9].

There is no consensus agreement about Ta/bone biocompatibility. Indeed, researchers reported that Ta could cause fibroblast inhibition [10]. However, according to the literature, Ta is recognized as a potential for clinical translation to treat biomaterial-associated infections [11] because of its outstanding *in vivo* biocompatibility, antimicrobial activity, and antiosteolytic effect. Recently, tantalum's osseointegration success was further supported by the study of Gee et al. [12]. They found no evidence of any inhibitory effect on the proliferation or cellular morphology of any of the human cell lineages studied. Besides, Ta and its compounds (oxides, nitrides, and carbides) showed simultaneously low ion release and high corrosion resistance [2,11,13-16] as well as a good potential for coatings, as they possess mechanical properties similar to bones [17]. However, the relatively high cost of manufacture and inability to produce a complete modular Ta implant has limited its widespread applicability [18].

Nowadays, it is of crucial importance to ensure high levels of safety and health in the products (prosthesis for biomedical applications) to be placed on the market. So, the goal of this work is to bring ideas to the market of biomedical products (implants and prostheses). That is why in this work a multilayer coating based on alternating bilayers $(ZrN/Ta)_n$ was deposited on Ti-6Al-4 V alloy by RF magnetron sputtering. While the ZrN top layer should guarantee the tribocorrosion performance, the ductility would be ensured by the Ta interface layer, which at the same time should ensure good ZrN/Ta interface adhesion. The goals and objectives are essentially (i) to evaluate simultaneously, the resistance of the coatings against the synergistic effect of wear (rubbing against alumina matter) and corrosion (electrochemical attacks of the aggressive Hank's solution) (ii) to understand the underlying mechanism responsible for the improvement of wear resistance in this kind of biotribocorrosion systems. Experimental parameters are chosen based on the literature review and previous laboratory work.

2. Experimental details

2.1. Synthesis of coatings

Zirconium nitride and tantalum films were realized by RF magnetron sputtering technique (NORDIKO type 3500). The metallic targets of Ta and Zr (disk of 101.6 mm of diameter, 3 mm thick, and a 99.98% purity) were used. Ti-6Al-4 V substrates were prepared for nanoindentation and tribocorrosion tests (Φ=20 mm x 5 mm discs, $R_a = 165 \pm 5$ nm). Silicon (100) wafer substrates (10 mm x 10 mm x 0.38 mm) were used for non-destructive analysis (thickness, residual stress, XRD). Coated Si substrates were cut longitudinally with a diamond tip for cross-section SEM observations. The Ti-6Al-4 V and Si (100) substrates were ex-situ ultrasonically cleaned for 10 min in acetone and deionized water successively before depositions. In each experiment, the sample holder of the sputtering reactor contains simultaneously five (5) Ti-6Al-4 V and five (5) silicon substrates

Prior to deposition, the targets and substrates were cleaned by Ar^+ ion bombardment for 5 min. The deposition process was conducted as fellow: the substrate was initially coated with pure Zr for 10 min under pure Ar flow to act as an interfacial layer and improve the adhesion strength between the substrate and the coating. After that, alternating (Ta/ZrN) layers were performed by controlling the reactive nitrogen flow. The Zr and Ta targets are introduced simultaneously in the reactor. When sputtering the Zr target, the process was conducted with a continuous mixing gas flow (Ar + N*)* ensured by an MKS Instruments mass-flow controller (Ar purity: 99.995 and N_2 purity: 99.999%). After that, nitrogen flow is stopped and completely removed from the chamber. The next step is the period of pure Ta sputtering, then re-sputtering of the Zr target takes place again in the reactive atmosphere (N_2) and the process is repeated. The N_2 flow rate was 0.6 sccm, kept constant for the ZrN layer while the Ar flow rate varies in the range (8–10) sccm. The deposition process was carried out without heating the substrates. Deposition parameters are summarized in Table 1.

The target bias voltage of −900 V was the best bias voltage to improve coating quality based on previous experiments [19]. The different multilayers coatings studied in this work are represented in Fig. 1. The selected architectural design of multilayer coatings has been made taking into account the reviewed literature, previous works, and experience. Based on preliminary tests, in order to optimize the deposition parameters, the total thickness of the multilayers has been chosen to be from 3.0 to 3.5 μm. Besides multilayer coatings studied in this work, alternating successively hard/ductile material are a biomimetic design inspired by the nature (nacre-inspired materials) [20–21].

The choice of the structure of the coating labeled M1, with layers of ZrN and Ta of equal thickness, is a classical architecture and has been made as a reference. The bilayer (ZrN/Ta) is constituted by $h_{\text{(hard phase)}} = h_{\text{(soft phase)}}$, h where thickness *i.e.* the thickness of the bilayer period (ZrN/Ta) is $h_{\text{(ZrN/Ta)}}$ =500 nm. A gradual decrease and gradual increase in the bilayer thickness are adopted in the coatings labeled M2 and M3 specimens as presented in Fig. 1.

2.2. Microstructural analysis

A field emission scanning electron microscope (SEM FEG; JEOL 7610F) equipped with an energy dispersive X-ray spectrometer (X-max 50 mm2 EDS detector; *Oxford Instruments*) was used to examine the surface morphologies and microstructures of specimens. During the EDS investigations, when the chemical composition of the surface and/or the depth profile were needed, the chamber pressure was in the range of 5.1 $\times 10^{-4}$ to 9.6 $\times 10^{-5}$ Pa, the accelerating voltage could vary from 5 to 15 kV, and the working distance (WD) was equal to 15 mm. While, during SEM morphology analysis, the working distance and the accelerating voltage are 6 to 7 mm and 5 kV, respectively.

Coating roughness on Ti-6Al-4 V and Si (100) substrates was determined using a 3D optical profilometer (*VEECO-Wyko NT-1100*) and an atomic force microscope AFM (*AFM Explorer, VEECO Topometrix*). The scanning area of each image was set at 5 μm × 5 μm with a scanning rate of 1.0 Hz to obtain a detailed surface image. The crystal structure of the synthesized coatings was analyzed by X-ray diffraction (XRD) using a (*Bruker, Germany)* diffractometer, with a radiation source CoKα (λ = 0.1789 Å). A continuous scan mode was used to collect 2θ data from 20° to 110°, at a scan rate of 1 °/min.

2.3. Mechanical properties

Hardness (H) and elastic (Young's) modulus (E), obtained from nanoindentation results, are the main parameters that characterize the mechanical properties of coatings. The resistance against plastic deformation can be evaluated by (H^3/E^2) ratio [22]. The high value of such a plasticity index (*i.e.*, high hardness and low elastic modulus) can indicate coatings with higher strength [23]. The second important factor is the H/E ratio, which indicated the elastic strain to failure resistance of the coating. It could characterize the protective properties of coatings in terms of cracking, abrasive wear and serve as a ranking parameter for

Table 1
Process parameters of the coating's layers obtained by magnetron sputtering.

Film	Working Pressure. (Pa)	% Of gas			Target Applied Power (W)	Target Bias Voltage (V)
		Ar	Ar	N_2		
Zr	0.4	–	100	–	400	- 900
Ta	0.5	100	–	–	400	−900
ZrN	0.5	–	80	20	400	−900

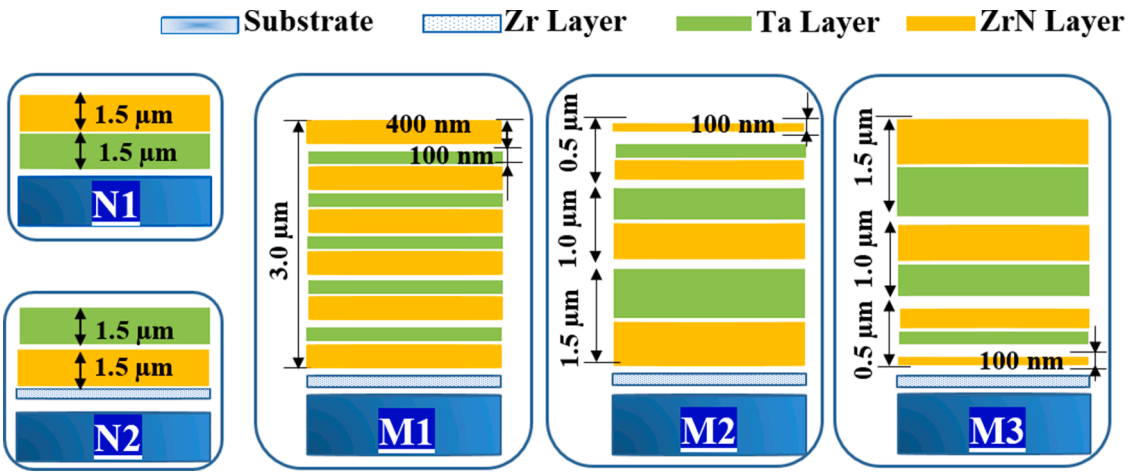

Fig. 1. Different multilayer designs studied in this work so-called N1, N2, M1, M2, and M3.

the toughness of the deposited films [24].

In this work, H and E parameters were determined through nano-indentation tests using an *MTS XP Nano Indenter* under a continuous stiffness measurement (CSM) mode and equipped with a Berkovich indenter. The indentation load-displacement data obtained in these tests were analyzed to obtain H and E, using the method of Oliver and Pharr [25]. Five to ten (05–10) tests were carried out for each sample. Each nanoindentation test was conducted to a maximum load of 14 mN. A constant strain rate of 0.05 s^{-1} was applied during loading and the penetration displacement was set to less than 10% of the total coating thickness (only less than 1% in the case of E calculation). The measured data was collected in depth *vs.* load hysteresis mode with an acquisition process controlled by penetration depth.

Obtained H represents an average value related to a specific penetration of the indenter. In other words, it represents a "total response" of the system. A bilayer coating is considered as the simplest multilayer coating, thus H has the same signification for all samples tested in this work.

2.4. Residual stress determination

Interferometry analysis is among several techniques developed for stress determination. The principle behind the method is to measure the curvature induced in the substrate due to stress in the film. Ardigo et al. [26]. described in detail how the curvature is related to the film stress and clarified some underlying assumptions used in interpreting the measurements.

The residual stress of the films was determined using Stoney's equation [26]:

$$\sigma_f = \frac{E_s}{6(1-\nu_s)}\frac{h_s^2}{h_f}\left(\frac{1}{R}-\frac{1}{R_0}\right) \quad (1)$$

where σ_f is the in-plane stress component in the film, h_f and h_s are the thickness of the film and substrate (h_{Si}= 380 µm), respectively. E_S, ν_s are the elastic modulus and the Poisson's ratio for the Si (100) substrate.

R and R_0 are the curvature radii of the substrate after and before deposition. They are measured by a 3D optical profilometer (*VEECO - Wyko NT-1100*) for both sides of the sample, considering the whole surface of the sample. The *Gwyddion* software was used to determine the values and the directions (negative or positive) of the radii of curvature [26]. The constant $Es/(1-\nu_s)$ ~1805 10^{11} N/m^2 for Si (100) substrate.

2.5. Scratch tests

The adherence study was carried out using a *Millennium 200 Scratch Tester*, equipped with a conical diamond tip (radius = 0.2 mm), to characterize the critical load at which failure occurs in dry conditions. The tangential force (Ft) was automatically recorded during the test, while the scratch marks were analyzed using an optical microscope. To verify the reproducibility of the results, three (03) scratch experiments were conducted on each tested samples. Test conditions are listed in Table 2

2.6. Tribocorrosion tests

The tests were performed using a three-electrode cell (Fig. 2). An Ag/AgCl electrode was used as a reference electrode; a platinum wire as the counter electrode and the sample was the working electrode. The tribocorrosion behavior of the samples was evaluated via the open circuit potential (OCP) and the coefficient of friction (COF) as a function of time (number of cycles) in a reciprocating sliding test using a conventional ball-on-disk tribometer (*TRIBOtester*). Before testing, each sample was immersed in 50 ml of Hank's solution in the three-electrode cell. The latest was carefully aligned to the ball holder in x, y and z axis. The test began after a 30 min stabilization time in the aggressive media before beginning the sliding test.

All tests were carried out in Hank's solution, a simulated body fluid commonly used in biomedical research for implant materials applications [27], at 37 ± 2 °C and maintained at pH 7.5 ± 0.5. The chemical composition of Hank's solution and the parameters of tribocorrosion tests are presented in table 3 and table 4, respectively. The operating conditions of the tribological test were selected based on a simulated hip joint, defined in terms of maximum contact pressure (~3 GPa).

2.7. Wear rate calculation

The sliding distance of 100 m was long enough to produce a breakdown of the coating. It corresponds to ~2000s. The specific wear rate was obtained by the classical formula as follows:

$$W_s = \frac{V}{NL}\left(mm^3 / Nm\right) \quad (2)$$

where W_s is the specific wear rate, V is the wear volume [mm^3], N is the normal load [N] and L is the sliding distance [m]. The W_s estimation was

Table 2
Scratch test conditions.

Contact geometry	Rockwell C
Load range	1 - 50 N
Load increase rate	79 N/min
Sliding velocity	8 mm/min
Scratch length	5 mm

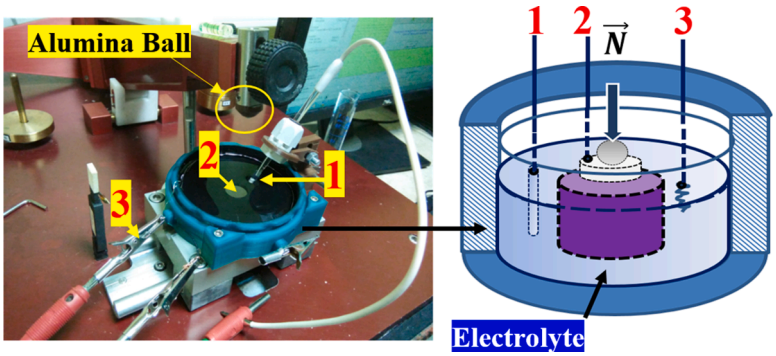

Fig. 2. Tribocorrosion apparatus. Labels (1), (2), and (3) indicate the counter electrode, working electrode, and reference electrode respectively. $\vec{N}$ is the applied normal load.

Table 3
Chemical composition of Hank's solution in [g/l].

NaCl	KCl	$MgSO_4 \bullet 7H_2O$	$CaCl_2.H_2O$	Na_2HPO_4	KH_2PO_4	$NaHCO_3$	Glucose
8.0	0.4	0.2	0.158	0.046	0.06	0.35	1.0

Table 4
Wear parameters for tribocorrosion tests performed in Hank's solution.

Velocity (cm/s)	1
Normal Force (N)	1
Time under load and OCP (s)	1800
Stroke (mm)	5
Temperature (°C)	25 ± 3
Relative Humidity (%)	40 ± 5
Al_2O_3 Ball (GPa) *Manufacture	*H = 16, E = 340

automatically obtained by software using a 3D profilometry image (*VEECO-Wyko NT1100*).

3. Results and discussion

3.1. Bilayer coatings

Fig. 3 shows SEM cross-section images with EDS profiles analysis and surface morphology of N1 and N2 coatings deposited on Si substrate. As expected, both Ta and ZrN layers present a columnar structure. Besides, EDS profiles confirm the chemical homogeneity (Fig. 3a and c). The microstructure of the Ta layers shows grains better defined with a sharp edge.

Surface morphology observations, of the upper layer surfaces, confirm that deposited films are rather homogenous with the presence of a granular morphology. Dense, refined, and regular grains having a rounded shape (domes) characterize the ZrN layer surface (Fig. 3b),

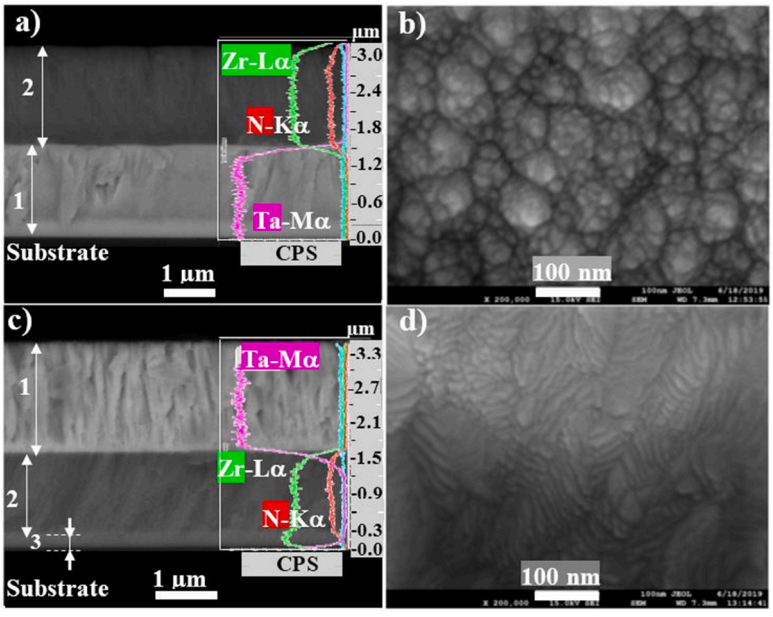

Fig. 3. SEM cross-section images and surface morphologies of N1 (a - b) and N2 (c - d) coatings, obtained on Si (100) substrate. Labels (1), (2), and (3) indicate Ta, ZrN, and Zr layers, respectively.

Table 5
Roughness, thickness and mechanical properties of the NI and N2 coatings deposited on Ti-6Al-4 V (*) and Si (**) substrates.

Coating	Roughness* ± 1.0 (nm)		Thickness** (μm)	σ** (GPa)	H* (GPa)	E* (GPa)
	Ra	Rq				
N1	16	22	3.15 ± 0.1	−0.98 ± 0.09	20 ± 2	230 ± 25
N2	21	27	3.3 ± 0.05	−1.7 ± 0.02	10 ± 1	186 ± 10

while grains in Ta layers showed an elongated shape (Fig. 3d). This surface appearance of Ta film was already observed [28].

Table 5 shows the intrinsic stress (σ) of N1 and N2 thin films on Si (100) wafers as well as H and E parameters. The N1 coating showed the highest mechanical properties when compared to N2. The film thickness (h_f) on the Si substrate was determined directly using SEM cross-section image of the coatings. The thickness of the N2 coating is equal to 3.3 μm while the N1 coating is 3.15 μm thick.

Roughness, in terms of arithmetical mean roughness (R_a) and root mean square (R_q) evaluated by optical profilometry indicates that there is no significant difference, and may be considered as in the same range.

Table 5 also shows a correlation between residual stress (σ) and mechanical properties (H, E) of the coatings. It is known that compressive stress increases coating hardness whereas tensile stress reduces it, as reported by [29]. All of the stress value, reported herein are compressive stresses ranging between ~−1 and - 1.8 GPa. Residual stress in N1 was more negative than that in N2. One can note that the hardness value of N1 is almost twice that for N2. Consequently, highest elastic strain to failure resistance factor ($H/E = 0.085$) as well as a plastic deformation resistance ($H^3/E^2 = 0.145$ GPa) of N1 samples were found superior to that of N2 ($H/E = 0.052$ and $H^3/E^2 = 0.026$ GPa), as expected. This is indicative of potential highest wear resistance of ZrN as the top layer [22,30-31]. Mechanical properties displayed in table 4 represent a basic criterion to evaluate the resistance to form debris during tribocorrosion tests. That is why ZrN was chosen as the top layer for M1, M2, and M3 multilayers.

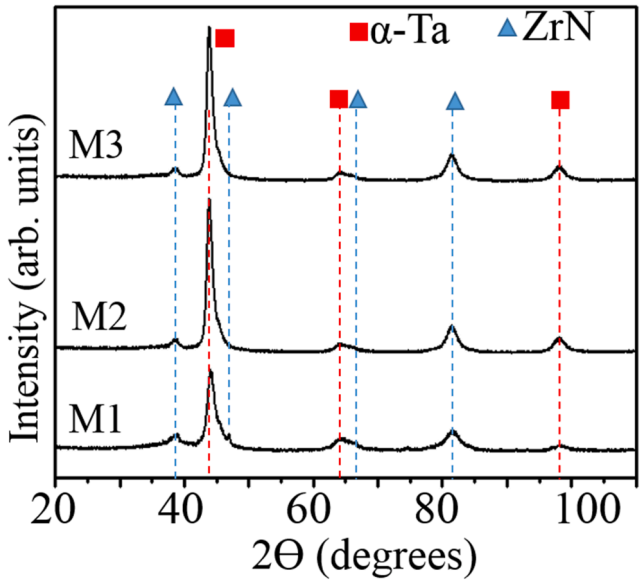

Fig. 4. XRD patterns of M1, M2, and M3 multilayers on Ti-6Al-4 V substrate.

3.2. Multilayer coatings

3.2.1. Microstructural and mechanical properties

The XRD patterns of the multilayer coatings are shown in Fig. 4. It presents two crystalline phases: the α-phase of tantalum (fcc crystal lattice) and a fcc-ZrN phase. All the multilayers (M1, M2, and M3) displayed a similar diffraction angle position for each noticeable peak. Peaks at 44.1°, 64.2°, 81.4° and 98.2° correspond respectively to (110), (200), (211) and (220) diffraction planes of fcc α-Ta phase in accordance with standard data file [© 2013 ICDD N° 00–004–0788]. Whereas peaks at 38.9°, 46.9°, and 66.1° are assigned respectively, to the (111), (200) and (220) the diffraction planes of fcc-ZrN phase [© 2013 ICDD N° 00–031–1493].

Fig. 5 shows cross-section views (a, b, and c) and AFM images (a', b', and c') of the deposited multilayer coatings on the silicon substrate. The total thickness of the deposited multilayer coatings, estimated by SEM and optical interferometric profilometry, was approximately 3.0 μm for all of the coatings. Clear contrast of alternating layers (Ta/ZrN) can be seen on SEM micrograph, *i.e.* each layer can be distinguished visibly (Fig. 5a-c). In addition to SEM micrograph, Fig. 5c shows the linear EDS scan for M3 specimen taken as an example.

AFM analysis is an important surface characterization technique to analyze the structure in the order of the nano range. It gives informative data on superficial microstructures such as roughness and the grain size parameters. Besides, one can see that the ZrN coating surfaces are composed of grains with globular domes.

It is noteworthy according to AFM (Table 6), that M2 and M3 present higher grain size than that of M1. Furthermore, M2 and M3 have better mechanical properties (H, E) than M1 Table 6. also presents the coating roughness evaluated by AFM analysis, thickness, and residual stress.

As one can see, AFM surface roughness values (R_a, R_q) can be assumed as being fairly similar. The M1 multilayer presents the lowest compressive stress. This result may be explained by the fact that in practice, numerous factors can influence the hardness and elastic modulus of sputtered coatings, *e.g.* presence of a soft amorphous phase, ion beam intermixing effects at the interfaces, interface roughening, substrate bias voltage, and so on [32].

It is known that two principal phenomena (among others) are responsible for controlling H and E. The first one is that smaller grains hinder the dislocation motion, leading to an expansion in hardness (Hall–Petch law). The second one is that more interfaces (interlayers) lead to high hardness and elastic modulus values. The high interface density contributes to impeding dislocation motion and the dislocation glide across the interfaces as explained by Caicedo et al. [33].

Data shown in Table 6 also reveal that on one hand, the grain size value of the ZrN coating in monolayer form ($h = 3.3$ μm) was slightly lower than grain size of M1 (ZrN top layer, $h = 400$ nm), while H of the monolayer coating was greater than H of the multilayer (large difference). On another hand, the grain size of the ZrN monolayer represents only half of those calculated for M2 and M3 *i.e.* 94 and 101 nm but a slight difference in H values was found with M2 and M3.

The influence of the bilayer period thickness on the hardness of multilayer coatings was investigated in the literature. A variety of mechanisms have been put forward and discussed to explain this change in mechanical properties. However, considerable care needs to be taken in interpreting literature data, depending on the deposition technique, deposition parameters, the type of multilayers, the measurement method employed, etc.

During the deposition of multilayer systems in this work, the change in the deposition conditions in order to grow the next layer requires the nucleation of new grains at the interface. This frequent re-nucleation controls the grain size and thus leads to a loss in crystallinity. For thinner multilayer periods, and the individual layers, lower grain size is demonstrated as observed by Lackner et al. [34]. on a $(Ti/TiN)_n$ multilayer system. Other authors [35] agree that the decrease in hardness observed in the multilayer coatings can be attributed to the alternating

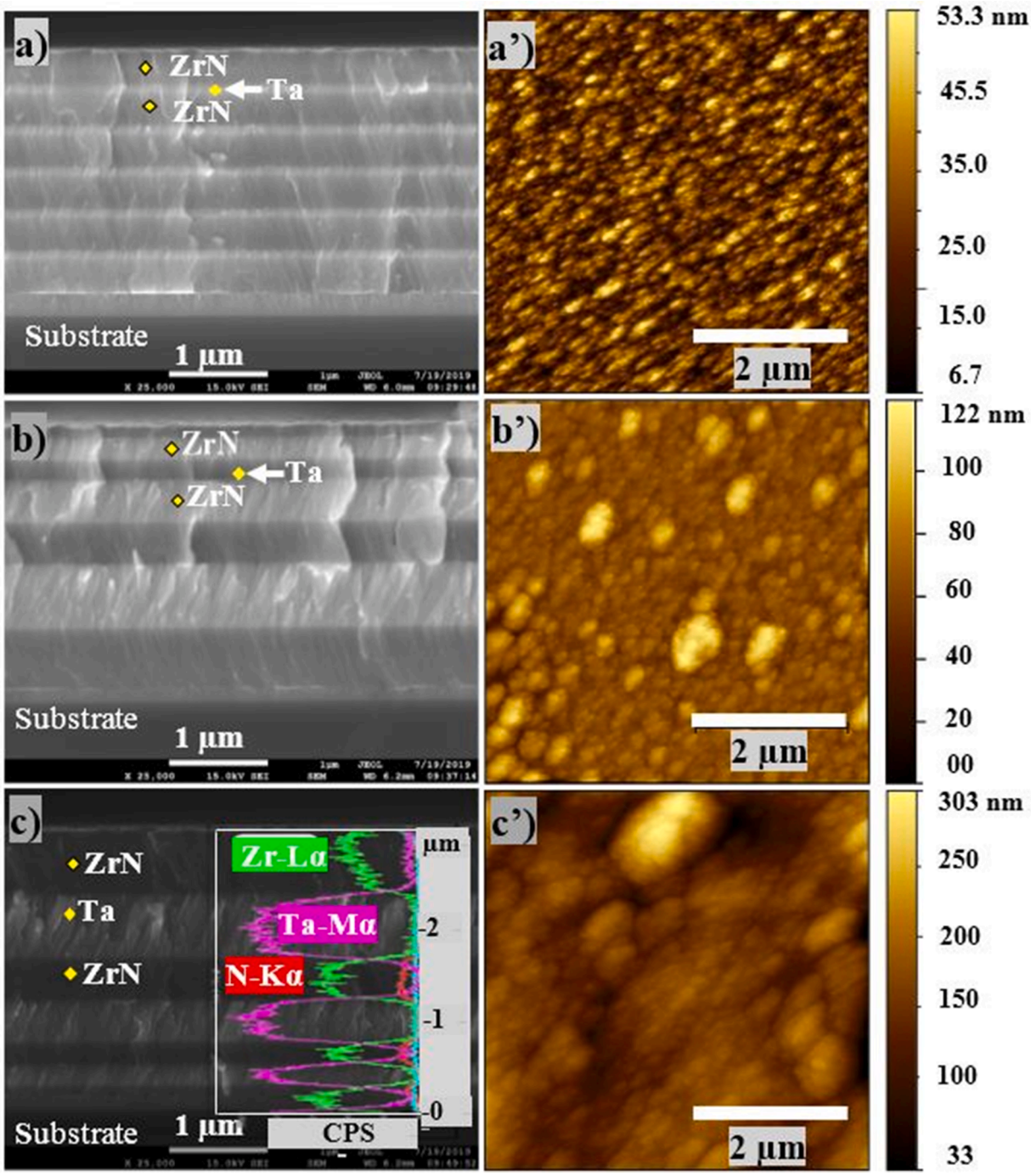

Fig. 5. SEM cross-section images of the M1 (a), M2 (b), and M3 (c) multilayer coatings. (a'), (b'), and (c') are the corresponding two-dimensional (2D) AFM images of the ZrN top layer.

Table 6
Roughness, thickness and mechanical properties of the M1, M2 and M3 multilayers ((*) Ti-6Al-4 V and (**) Si substrates).

Coating	**Thickness ± 0.01 (µm)	*Roughness (nm)		*Grain size (nm)	**σ (GPa) ± 0.01	*H (GPa) ± 0.5	*E (GPa) ± 5
		R_a ± 0.1	R_q ± 0.2				
M1	2.9	4.06	5.12	50 ± 3	−0.78	14	196
M2	2.91	6.2	7.8	94 ± 5	- 1.17	19	220
M3	2.94	6.83	8.59	101 ± 7	- 1.19	17	206
ZrN_{mono}	3.3	3.05	2.3	45 ± 5	−1.35	20	268

stress field, as the difference in the elastic properties of the two constituents (of the metallic/ceramic bilayer period) is significant as reported by Lattemann et al. [36]. While Hernández-Navarro et al. [37]. found most recently, opposite results *i.e.* H (multilayer) > H (monolayer) on a tri-layer system (ceramic/metallic/ceramic). Early investigations [38–41] have established that below certain values of layer thickness; dislocations are unable to multiply or to propagate from layer to layer, apparently hindered by strain coherency effects at layer interfaces. Of course, the density and quality of interfaces between the alternating single layers play a key role in controlling the grain size [42].

Unfortunately, no significant relationship between hardness and total thickness has been well established, especially when experimental errors were taken into account.

In the present case, regardless of the design, multilayer coatings (M1, M2, and M3) exhibit lower hardness (slightly) when compared to ZrN (monolayer) and the N1 bilayer coating (ZrN on Ta).

Despite the fact that σ and (H, E) parameters are measured by two different methods, and deposited on two different substrates, the direct influence of σ as the main dominant factor controlling H and E seems to be the suitable explanation of these results (σ of the monolayer was more negative −1.35 GPa than that of multilayer coatings). The H/E ratio of M1, M2, and M3 coatings were 0.074, 0.087, and 0.084 respectively (Table 6), indicating that all the films should have an acceptable resistance to plastic deformation and good wear resistance [30]. The M2 specimen is noteworthy for its highest mechanical properties compared to the others.

3.2.2. Scratch tests

Scratch testing is probably the most widely used test for assessing adhesion strength of coating-substrate systems as defined by P. Benjamin, and C. Weaver in 1960 [43]. However, obtained results are influenced by various factors such as coating thickness, substrate mechanical properties, and test conditions.

Fig. 6 presents the plot, representing the tangential force (F_t) as a function of increasing load (applied normal load (F_n)), and the optical micrograph of the scratch mark which allow to determining the critical load of cohesive (L_{C1}) and adhesive damage (L_{C2}) obtained in the case of M1 coating. L_{C1} is also called the lower critical load. It corresponds to the first crack event. L_{C2} (the higher critical load) is attributed to the first delamination of the coating with substrate exposure. As presented in Fig. 6, the load was increased linearly until the failure of the coating. The recorded results are L_{C1} (M1) = 6 ± 1 N and L_{C2} (M1) =17 ± 0.5 N.

The adhesion results of the M1 coating, shown in Fig. 6a, are taken as an example. Note that, all the other M2 and M3 multilayer coatings

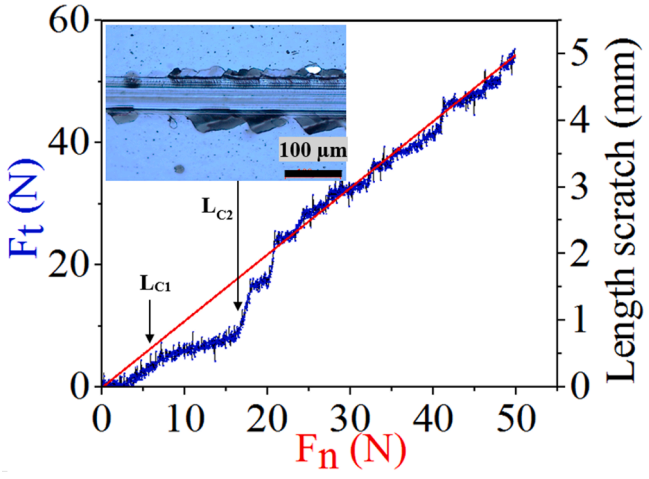

Fig. 6. (a) Scratch test result plot (Tangential force (F_t) *vs.* Normal load (F_n)) with critical loads (L_{C1}, L_{C2}) and optical microscopy image (b) of damaged M1 multilayer coating.

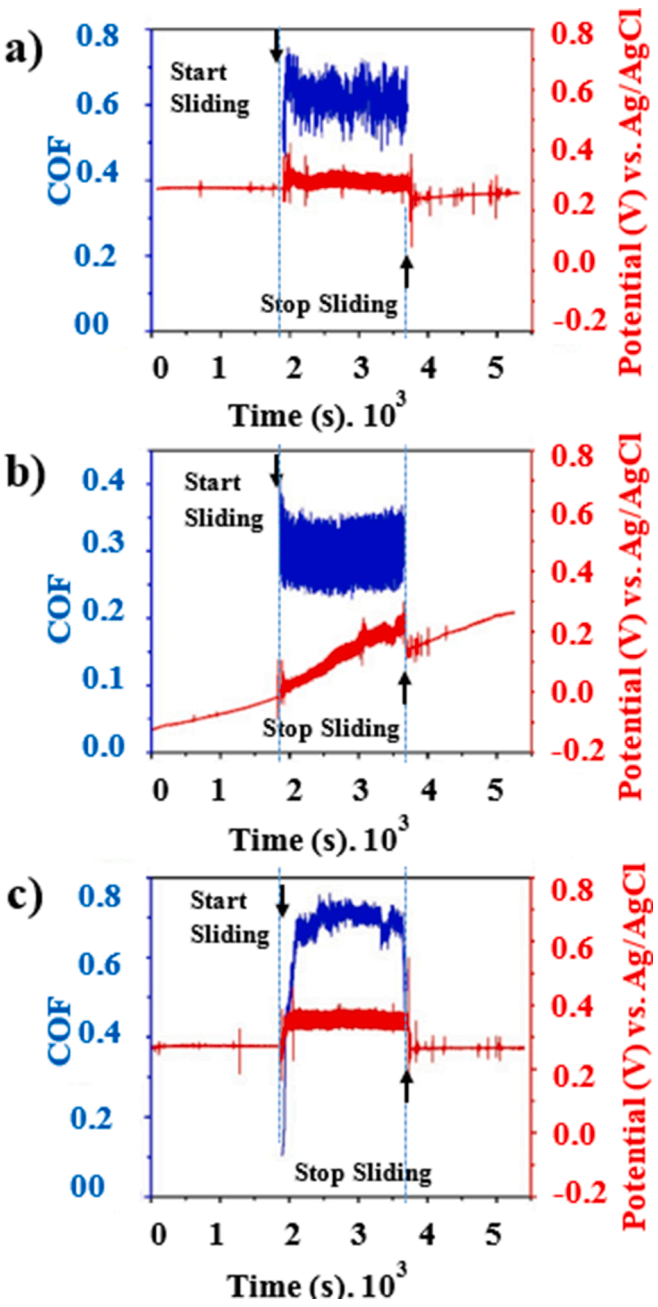

Fig. 7. COF and OCP evolution during tribocorrosion tests of M1 (a), M2 (b), and M3 (c) multilayers against alumina ball in Hank's solution.

exhibit similar scratch resistance. The cohesive strength values are L_{C1} (M2) = 10 ± 1 N and L_{C1} (M3) = 8 ± 1 N while the adhesive strength values are L_{C2} (M2) = 23 ± 0.5 N and L_{C2} (M3) = 21 ± 0.5 N. These results can be regarded as acceptable because the deposition process was carried out using a non-heated substrate [44].

3.2.3. COF and OCP evolution

Fig. 7 shows that M2 has a different tribocorrosion behavior than M1 and M3. At the onset sliding test the measured COF of M2 is stable and around 0.3 while the COF of M1 and M3 are higher around 0.61 and 0.66, respectively. As a consequence, M1 and M3 showed a similar curve tendency of the OCP evolution; the OCPs drastically shifted towards slightly more positive potential as sliding friction started, implying passive layer formation and thus no-corrosion tendency. The sudden increase and/or decrease of the corrosion current (inversely with the

corrosion potential) implies the removal and regeneration (reappearance) of the passive film [45].

Higher OCP values provide better resistance against corrosion. After 2.8 0.10^3 s for M1 and 2 . 10^3 s for M3, their potential remains stable until the end of the corrosion tests at ~0.3 and ~0.35 V *vs.* Ag/AgCl, respectively. At the end of the test, a drop in curves occurs towards initial OCP ~0.25 - 0.28 V *vs.* Ag/AgCl (Fig. 7a and 7c). However, the OCP evolution of M1 starts from −0.14 V *vs.* Ag/AgCl thus slightly and progressively increases. After sliding, the potential was restored to a higher value than the initial one (~0.22 V *vs.* Ag/AgCl). The OCP tendency showed here in all cases is a sign that a high quality passive film is continuously formed during sliding tests in Hank's solution. It was reported that in a multilayered system, the ending layer largely influences the corrosion behavior [46]. Therefore, the topmost layer thickness probably influences the corrosion mechanisms evolved during tribocorrosion tests.

3.2.4. *Specific wear rate calculation*

Specific wear rate (Ws), estimated from the wear volume (or volume loss) is the main factor employed to quantify wear damage. The lower the specific wear rate, the more wear resistant the coating. In this context Ws estimation produced by sliding tests under applied OCP of M1, M2, and M3 multilayers are 5.65, 0.212, and 5.38. 10^{-5} mm^3/N.m, respectively. These results confirm that the multilayer M2, presenting the highest H/E (0.087) and $H^3/E^2 = 0.15$ GPa ratios, also presents the highest wear resistance. As a result, the wear rate estimation confirms the best tribocorrosion performance of the M2 multilayer. This is a significant result for biomedical devices because a low wear resistance leads to the release of wear debris, and thus to inflammation and failure of the prosthesis [47].

3.2.5. *Wear mechanisms*

Fig. 8 shows the results of SEM/EDS analysis of the wear tracks obtained on the three multilayers after tribocorrosion tests. No adhered material was shown on any of the analyzed wear tracks. According to

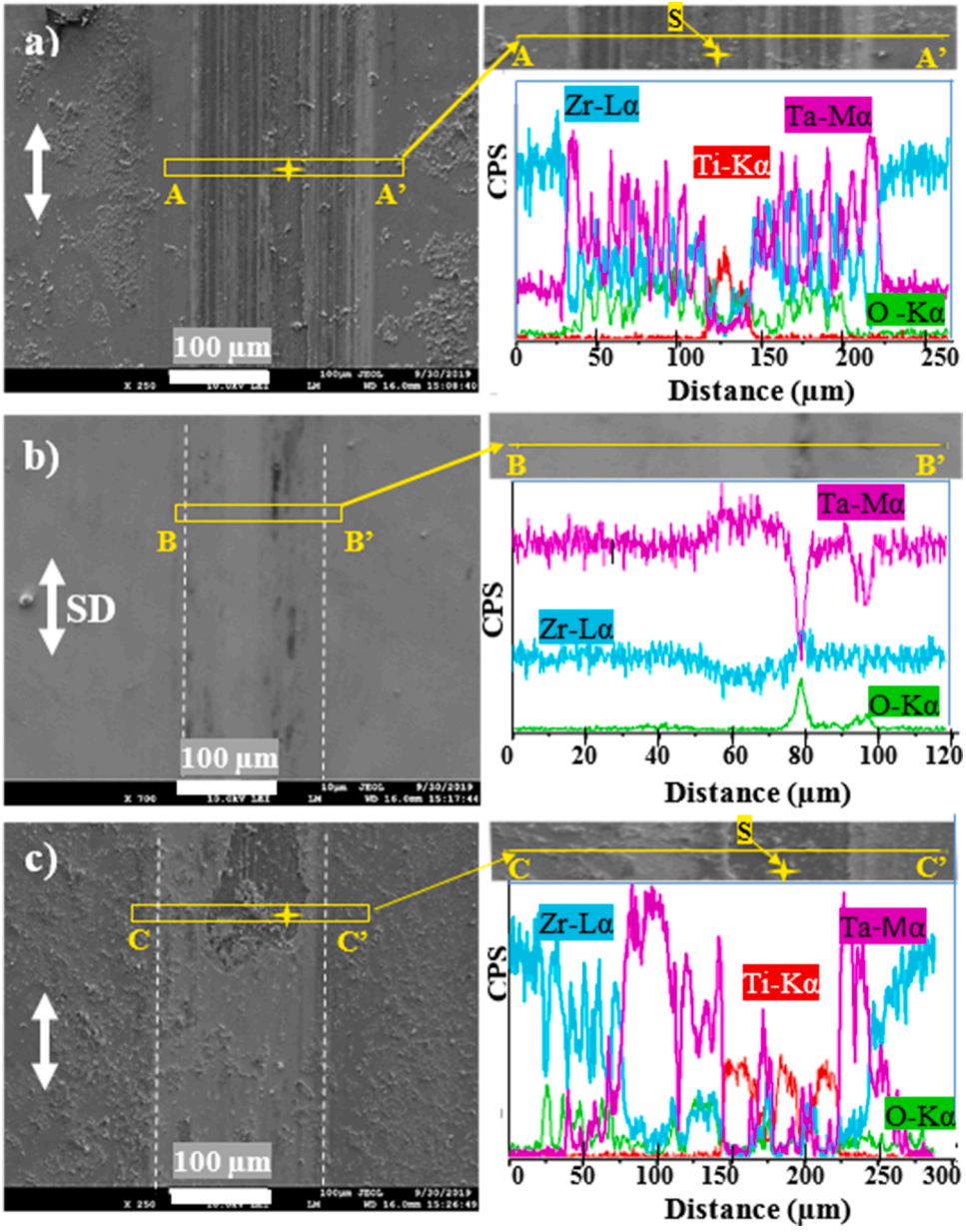

Fig. 8. SEM images of the wear tracks after tribocorrosion tests of M1 (a), M2 (b), and M3 (c) multilayers and corresponding EDS profiles on AA', BB' and CC' lines (S-substrate).

EDS profiles, rich O element in the sliding area showed that oxidization occurred in contact during sliding, which could be attributed to temperature rise at the contact surfaces.

The M1 multilayer (Fig. 8a) showed parallel stripes and wear debris inside the wear track, probably coming from abrasive wear damage. Besides, the coating was destroyed entirely in the center of the wear track (maximal pressure) as indicated by label S (Substrate). The wear track of the M3 multilayer presented a big delamination area as shown in Fig. 8c. Indeed, titanium (coming from the substrate) appears across the whole width of the wear track on the EDS profile.

Finally, the M2 multilayer presents a smooth surface morphology in its tribocorrosion track. Hardly perceptible shallow furrows caused by mild abrasive wear were the consequence of better wear resistance. No coating delamination nor deep stripes are observed. Besides, the residual coating (from M2) was not destroyed entirely as in the case of M1 and M3. The EDS profile of the wear track reveals that coating chemical elements such as Ta and Zr are still present. Fine scratches (10–20 μm in length, parallel to the sliding direction (S.D) were probably produced by particles of wear debris, but not deep enough to reach the substrate, are observed.

Since all the multilayers have been tested in the same conditions, it is possible to consider that all of them suffer identical synergistic effect of two damage mechanisms simultaneously (wear and corrosion). As a consequence, the possible scenario maybe occurred as follows (Fig. 9).

Three principal steps seem to characterize the wear process: (i) rubbing under applied OCP (and normal load) provokes thinning of the coating covered by a tribocorrosion layer, thus leading to cracks and rifts, (ii) fragments are formed and detached (coating delamination) and the electrolyte reaches the substrate, (iii) deterioration of the surface substrate.

3.2.6. Discussion

After the tribocorrosion test (2000s), wear scars of multilayers showed different states of wear resistance (Fig. 8). M1 reached the third step, M3 presented signs of the second step while M2 has not reached the first step so far. When the tribocorrosion test began, the sample immersed in Hank's solution was immediately covered by a passive film as revealed by OCP measurements (Fig. 7a-c). Simultaneously the alumina ball started to rub against the ZrN (topmost layer), abraded it by means of asperities, and leaving an active area behind. Therefore, after more and more sliding cycles, a tribocorrosion layer can entirely cover the coating surface. On one hand, the wear track results in the "load/unload" cycles appearance. On the other hand, the "partial removal/renewing layer formation" occurs. Consequently, fatigue may lead to nucleation and propagation of sub-surface cracks.

The Ta layer, just below the ZrN top layer of M2 (only 100 nm thick) is reached earlier than in the case of M1 and M3 (Fig. 1). In other words, Ta layer/alumina ball contact (in M2) occurs at the same time when ZrN layer/alumina ball contact still takes place in M1 and M3. It is possible to suppose that the first wear debris formation possibly acts as "solid lubricant" in the M2 case (hard and brittle particles diminish friction forces), but act as "abrasive particles" in the M1 and M3 cases, because of their low H/E ratio, leading to a fast coating deterioration. Elasto-plastic properties of the adjacent surfaces are a key factor in the wear mechanism since they are closely related to the energy dissipation and the toughness of the near-surface region.

The second step starts after cracks and rifts formation. Then, the corrosive media has diffused underneath the coating, provoked local anodic (worn)/cathodic (passive) areas, namely corrosion of the substrate, and led to the third and final step of film detachment and scratch the surface of the substrate.

Finally, tribocorrosion layer formation is a mixture between passive layer (automatic formation at the immersion time in aggressive media) and oxide layer (formation due to rubbing/increasing in temperature) seems to be the main parameter controlling the wear mechanism.

4. Conclusion

Multilayer coatings consisting of alternating pure Ta metallic and ceramic ZrN layers with different thickness designs were deposited on Ti-6Al-4 V biomedical alloy using magnetron sputtering. XRD analysis revealed only the presence of α-Ta and ZrN crystalline phases in all the studied coatings. The $(Ta/ZrN)_n$ multilayer labeled M2, showed the best tribocorrosion performances as it presents a lower friction coefficient and lower specific wear rate. This coating seems the most suitable material for use in biomedical applications. These performances are related to: (i) its higher mechanical properties carried out from nanoindentation experiments and, (ii) its architectural thickness design. During tribocorrosion tests, the potential rose to more noble values, indicating that all of the coatings behave well against corrosion, however, they underwent different wear damages. Under selected conditions of tribocorrosion tests, the synergistic effect of wear against alumina ball and

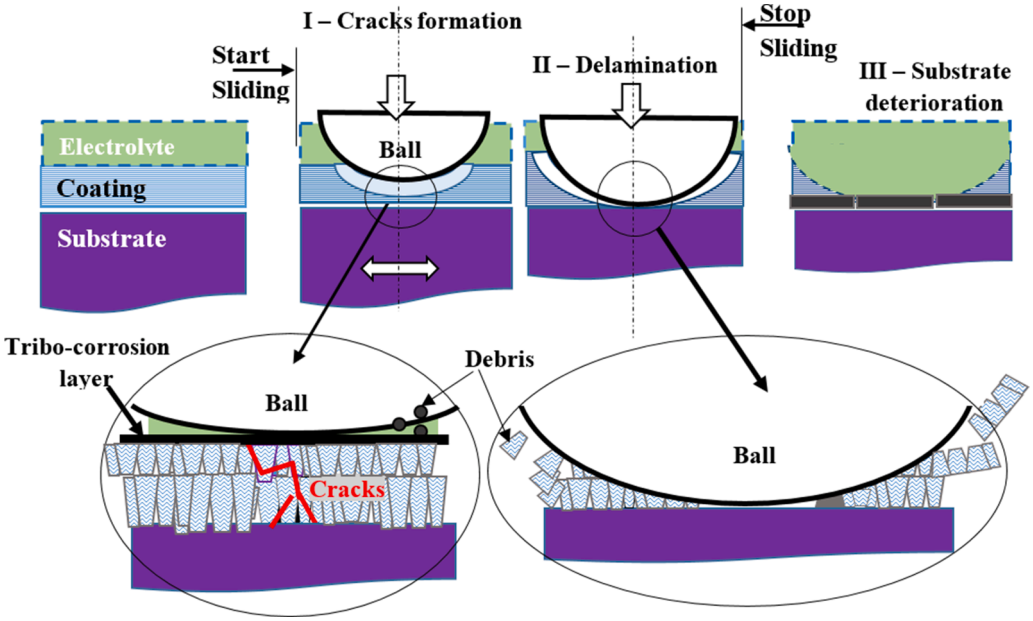

Fig. 9. Schematic diagram of the possible wear mechanisms evolving during the tribocorrosion test.

corrosion under OCP in Hank's solution leads to complete deterioration of the multilayer coating having the lowest H/E ratio. The multilayer having the highest H/E ratio was more resistant with minimum damage. These results are of great importance in manufacturing orthopedic prosthesis for long time service, as the health of patients and the service life of the prosthesis are the fundamental priorities.

Credit author statement

Nasser Eddine BELIARDOUH: Conceptualization, Supervision, Writing- Original draft. Chems Eddine RAMOUL: Conceptualization, Investigation, Data curation. Corinne NOUVEAU: Conceptualization, Supervision, Review. Hakan KALELI Conceptualization, Supervision, review and Alex MONTAGNE: Investigation, Data curation

Funding

This research did not receive any specific grant from funding agencies in the public, commercial, or not-for-profit sectors.

Declaration of Competing Interest

The authors declare that they have no competing interests.

Acknowledgements

The authors are gratful to the Directorate General For Scientific Research and Technological Development (DGRSDT) at the Algerian Ministry of Higher Education and Scientific Research (MESRS) for its support. The authors are also gratful to Mr. Denis Lagadrillère for his MEB/EDS competencies.

References

[1] M.J. Runa, M.T. Mathew, L.A. Rocha, Tribocorrosion response of the Ti6Al4V alloys commonly used in femoral stems, Tribol. Int. 68 (2013) 85–93, http://dx.doi.org/10.1016/j.triboint.2013.09.022.

[2] C. Balagna, M.G. Faga, S. Spriano, Tribological behavior of a Ta-based coating on a Co–Cr–Mo alloy Surf, Coat. Technol. 258 (2014) 1159–1170, http://dx.doi.org/10.1016/j.surfcoat.2014.07.016.

[3] O. Çomaklı, Improved structural, mechanical, corrosion and tribocorrosion properties of Ti45Nb alloys by TiN, TiAlN monolayers, and TiAlN/TiN multilayer ceramic films, Ceram. Int. 47 (3) (2021) 4149–4156, https://doi.org/10.1016/j.ceramint.2020.09.292.

[4] R. Bahi, C. Nouveau, N.E. Beliardouh, C.E. Ramoul, S. Meddah, O. Ghelloudj, Surface performances of Ti-6Al-4V substrates coated PVD multilayered films in biological environments, Surf. Coat. Technol. 385 (2020), 125412, https://doi.org/10.1016/j.surfcoat.2020.125412.

[5] A.M. Echavarria, P.M. Rico Tortosa, J.L. Gómez Ribelles, M.A. Pacha-Olivenza, M. Fernandez-Calderon, G. Bejarano-G, Development of a Ta/TaN/$TaN_x(Ag)_y$/TaN nanocomposite coating system and bio-response study for biomedical applications, Vacuum 145 (2017) 55–67, https://doi.org/10.1016/j.vacuum.2017.08.020.

[6] J. Min-Kyung, P. Sang-Won, L. Kwangmin, K. In-Chol, Y. Kwi-Dug, K. Hyun-Seung, Evaluation of antibacterial activity and osteoblast-like cell viability of TiN, ZrN and (Ti1-xZrx)N coating on titanium, J. Adv. Prosthodont. 7 (2015) 166–171, https://doi.org/10.4047/jap.2015.7.2.166.

[7] X.M. Zhang, Y. Li, Y.-X. Gu, C.-N. Zhang, H.-C. Lai, J.-Y. Shi, Ta-coated titanium surface with superior bacteriostasis and osseointegration, Int. J. Nanomedicine 14 (2019) 8693–8706, https://doi.org/10.2147/IJN.S218640.

[8] T. Kuznetsova, V. Lapitskaya, A. Khabarava, S. Chizhik, B. Warcholinski, A. Gilewicz, The influence of nitrogen on the morphology of ZrN coatings deposited by magnetron sputtering, Appl. Surf. Sci. 522 (2020), 146508, https://doi.org/10.1016/j.apsusc.2020.146508.

[9] M.A. Auger, J.J. Araiza, C. Falcony, O. Sanchez, J.M. Albella, Hardness and tribology measurements on ZrN coatings deposited by reactive sputtering technique, Vacuum 81 (2007) 1462–1465.

[10] R. Jordan, A. Saithna, J. Paxton, L. Grover, P. Thompson, S. Krikler, Early failure of Tantalum patellar arguments in the post-Patellectomy Knee, Curr. Orthop. Pract. 25 (5) (2014) 472–477, https://doi.org/10.1097/BCO.0000000000000139.

[11] S. Konan, C.P. Duncan, B.A. Masri, D.S. Garbuz, Porous tantalum uncemented acetabular components in revision total hip arthroplasty: a minimum ten-year clinical, radiological and quality of life outcome study, Bone Joint J. 98-B (2016) 767–771, https://doi.org/10.1302/0301-620X.98B6.37183.

[12] E.C.A. Gee, R. Eleotério, L.M. Bowker, J-A.Hunt A.Saithna, The influence of tantalum on human cell lineages important for healing in soft-tissue reattachment surgery: an *in vitro* analysis, J. Exp. Orthop. 6 (40) (2019) 2–6, https://doi.org/10.1186/s40634-019-0210-8.

[13] M. Alishahi, F. Mahboubi, S.M. Musavi Khoei, M. Aparicio, E. Lopez-Elvira, J. Méndez, R. Gago, Structural properties and corrosion resistance of tantalum nitride coatings produced by reactive DC magnetron sputtering, RSC Adv 6 (92) (2016) 89061–89072, http://dx.doi.org/10.1039/c6ra17869c.

[14] C. Yang, J. Li, C. Zhu, Q. Zhang, J. Yu, J. Wang, Q. Wang, J. Tang, H. Zhou, H. Shen, Advanced antibacterial activity of biocompatible tantalum nanofilm via enhanced local innate immunity, Acta Biomater 89 (2019) 403–418, https://doi.org/10.1016/j.actbio.2019.03.027.

[15] A.C. Hee, Y. Zhao, S.-.S. Jamali, A. Bendavid, P.-.J. Martin, H. Guo, Characterization of tantalum and tantalum nitride films on Ti6Al4V, Surf. Coat. Technol. 365 (2018) 24–32, https://doi.org/10.1016/j.surfcoat.2018.05.007.

[16] J.J. Lai, Y.S. Lin, C.H. Chang, T.Y. Wei, J.C. Huang, Z.X. Liao, C.H. Lin, C.H. Chen, Promising Ta-Ti-Zr-Si metallic glass coating without cytotoxic elements for bio-implant applications, Appl. Surf. Sci. 427 (2018) 485–495, https://doi.org/10.1016/j.apsusc.2017.08.065.

[17] H.A. Ching, D. Choudhury, M.-.J. Nine, N.A. Abu Osman, Effects of surface coating on reducing friction and wear of orthopaedic implants, Sci. Technol. Adv. Mater. 15 (1) (2014), 014402, https://doi.org/10.1088/1468-6996/15/1/014402.

[18] S. Dittrick, V.K. Balla, S. Bose, A. Bandyopadhyay, Wear performance of laser processed tantalum coatings, Mater Sci Eng C 31 (8) (2011) 1832–1835, https://doi.org/10.1016/j.msec.2011.08.017.

[19] C. Ramoul, N.E. Beliardouh, R. Bahi, C. Nouveau, A. Djahoudi, M.J. Walock, Surface performances of PVD ZrN coatings in biological environments, Tribol Mater Surf Interfaces 13 (1) (2018) 12–19, https://doi.org/10.1080/17515831.2018.1553820.

[20] T. Graham, M. Sarikaya, Growth dynamics of red abalone shell: a biomimetic model, Mater. Sci. Eng. C 11 (2000) 145–153, https://doi.org/10.1016/S0928-4931(00)00202-2.

[21] Z. Qin, L. Dimas, D. Adler, G. Bratzel, M.-.J. Buehler, Biological materials by design, a review, J. Phys. Condens. Matter. 26 (2014), 073101, https://doi.org/10.1088/0953-8984/26/7/073101.

[22] A. Leyland, A. Matthews, On the significance of the H/E ratio in wear control: a nanocomposite coating approach to optimised tribological behaviour, Wear 246 (2000) 1–11, https://doi.org/10.1016/S0043-1648(00)00488-9.

[23] Artur Wiatrowski, Michał Mazur, Agata Obstarczyk, Damian Wojcieszak, Danuta Kaczmarek, Jerzy Morgiel, Gibson Des, Comparison of the physicochemical properties of TiO2 thin films obtained by magnetron sputtering with continuous and pulsed gas flow, Coatings 8 (2018) 412, https://doi.org/10.3390/coatings8110412.

[24] B.O. Postolnyi, V.M. Beresnev, G. Abadias, O.V. Bondar, L. Rebouta, A.D. Pogrebnjak J.P.Araujo, Multilayer design of CrN/MoN protective coatings for enhanced hardness and toughness, J. Alloys Compd. (2017), https://doi.org/10.1016/j.jallcom.2017.07.010.

[25] W.C. Oliver, G.M. Pharr, An improved technique for determining hardness and elastic modulus using load and displacement sensing indentation experiments, J. Mater. Res. 7 (06) (1992) 1564–1583, https://doi.org/10.1557/JMR.1992.1564.

[26] M.R. Ardigo, M. Ahmed, A. Besnard, Stoney formula: investigation of curvature measurements by optical profilometer, Adv. Mater. Res. 996 (2014) 361–366, https://doi.org/10.4028/www.scientific.net/AMR.996.361.

[27] S. Calderon, C.F. Almeida Alves, N.K. Manninen, A. Cavaleiro, S. Carvalho, Electrochemical corrosion of nano-structured magnetron-sputtered, coatings, a review, Coatings 9 (2019) 682–710, https://doi.org/10.3390/coatings9100682.

[28] H. Ren, M. Sosnowski, Tantalum thin films deposited by ion assisted magnetron sputtering, Thin Solid Films 516 (2008) 1898–1905, https://doi.org/10.1016/j.tsf.2007.10.127.

[29] G.C.A.M. Janssen, M.M. Abdalla, F. Van Keulen, B.R. Pujada, B. Van Venrooy, Celebrating the 100th anniversary of the Stoney equation for film stress: developments from polycrystalline steel strips to single crystal silicon wafers, Thin Solid Films 517 (2009) 1858–1867, https://doi.org/10.1016/j.tsf.2008.07.014.

[30] A. Leyland, A. Matthews, Design criteria for wear-resistant nanostructured and glassy-metal coatings, Surf. Coat. Technol. 177–178 (2004) 317–324, https://doi.org/10.1016/j.surfcoat.2003.09.011.

[31] M.E. Roy, L.A. Whiteside, J. Xu, B.J. Katerberg, Diamond-like carbon coatings enhance the hardness and resilience of bearing surfaces for use in joint arthroplasty, Acta. Biomater. 6 (2010) 1619–1624, https://doi.org/10.1016/j.actbio.2009.10.037.

[32] H.C. Barshilia, A. Jain, K.S. Rajam, Structure, hardness and thermal stability of nanolayered TiN/CrN multilayer coatings, Vacuum 72 (2004) 241–248, https://doi.org/10.1016/j.vacuum.2003.08.003.

[33] J.C. Caicedo, C. Amaya, L. Yate, M.E. Gómez, G. Zambrano, J. Alvarado-Rivera, TiCN/TiNbCN multilayer coatings with enhanced mechanical properties, Appl. Surf. Sci. 256 (2010) 5898–5904, https://doi.org/10.1016/j.apsusc.2010.03.071.

[34] J.M. Lackner, Industrially-scaled room-temperature pulsed laser deposition of Ti-TiN multilayer coatings, in: Eight International Conference on Laser Ablation; J. Phys. Conf. Ser. 59, 2007, pp. 16–21, https://doi.org/10.1088/1742-6596/59/1/004.

[35] Z. Zhang, O. Rapaud, N. Allain, D. Mercs, M. Baraket, C. Dong, C. Coddet, Characterizations of magnetron sputtered CrSiN/ZrN multilayer coatings— from structure to Tribological behaviors, Adv. Eng. Mater. 11 (8) (2009) 667–673, https://doi.org/10.1002/adem.200900051.

[36] M. Lattemann, S. Ulrich, Investigation of structure and mechanical properties of magnetron sputtered monolayer and multilayer coatings in the ternary system Si–B–C, Surf. Coat. Technol. 201 (2007) 5564–5569, https://doi.org/10.1016/j.surfcoat.2006.07.130.

[37] C. Hernández-Navarro, L.P. Rivera, M. Flores, E. Camps, S. Muhl, E. Garcia, Tribological study of a mono and multilayer coating of TaZrN/TaZr produced by magnetron sputtering on AISI-316L stainless steel, Tribol. Int. 131 (2019) 288–298, https://doi.org/10.1016/j.triboint.2018.10.034.
[38] J.S. Koehler, Attempt to design a strong solid, Phys. Rev. B2 (1970) 547–551, https://doi.org/10.1103/PhysRevB.2.547.
[39] S.L. Lehoczy, Strength enhancement in thin-layered Al-Cu laminates, J. Appl. Phys. 49 (1978) 5479–5485, https://doi.org/10.1063/1.324518.
[40] S.L. Lehoczy, Retardation of dislocation generation and motion in thin-layered metal laminates, Phys. Rev. Lett. 41 (1978) 1814–1818, https://doi.org/10.1103/PhysRevLett.41.1814.
[41] U. Helmersson, S. Todorova, S.A. Barnett, J.-.E. Sundgren, L.C. Markert, J. E. Greene, Growth of single crystal TiN/VN strained-layer super lattices with extremely high mechanical hardness, Appl. Phys. 62 (2) (1987) 481–484, https://doi.org/10.1063/1.339770.
[42] Y.X. Oua, H.Q. Wang, B. Liao, M.K. Lei, X.P. Ouyang, Tribological behaviors in air and seawater of CrN/TiN superlattice coatings irradiated by high-intensity pulsed ion beam, Ceram. Int. 45 (2019) 24405–24412, https://doi.org/10.1016/j.ceramint.2019.08.162.
[43] P. Benjamin, C. Weaver, Measurement of adhesion of thin films, Proc. R. Soc. Proc. R. Soc. A 254 (1960) 163–176, https://doi.org/10.1098/rspa.1960.0012.
[44] Ay Ching Hee, Philip J. Martin, Avi Bendavid, Sina S. Jamali, Yue Zhao, Tribo-corrosion performance of filtered-arc-deposited tantalum coatings on Ti-13Nb-13Zr alloy for bio-implants applications, Wear 400–401 (2018) 31–42, https://doi.org/10.1016/j.wear.2017.12.017.
[45] C. Wenfang, C. Jun, L. Zhongyuan, Bio-tribocorrosion behavior of a nanocrystalline TiZrN coating on biomedical titanium alloy, Surf. Coat. Technol. 369 (2019) 79–86, https://doi.org/10.1016/j.surfcoat.2019.04.036.
[46] M. Fenker, M. Balzer, H. Kappl, Corrosion behaviour of decorative and wear resistant coatings on steel deposited by reactive magnetron sputtering— Tests and improvements, Thin Solid Films 515 (2006) 27–32, https://doi.org/10.1016/j.tsf.2005.12.020.
[47] R. MT Raimondi, Pietrabissa The in-vivo wear performance of prosthetic femoral heads with titanium nitride coating, Biomaterials 21 (9) (2000) 907–913, https://doi.org/10.1016/S0142-9612(99)00246-X.